ACS APPLIED NANO MATERIALS

www.acsanm.org Article

Self-Assembled Multiphase Nanocomposite $SrCo_{1-x}Fe_xO_{3-\delta}$ Thin Films with Voltage-Controlled Magnetism for Spintronic Applications

Eunsoo Cho, Abinash Kumar, Shuai Ning,* James M. LeBeau, and Caroline A. Ross*

Cite This: *ACS Appl. Nano Mater.* 2022, 5, 14646−14653 Read Online

ACCESS | Metrics & More | Article Recommendations | Supporting Information

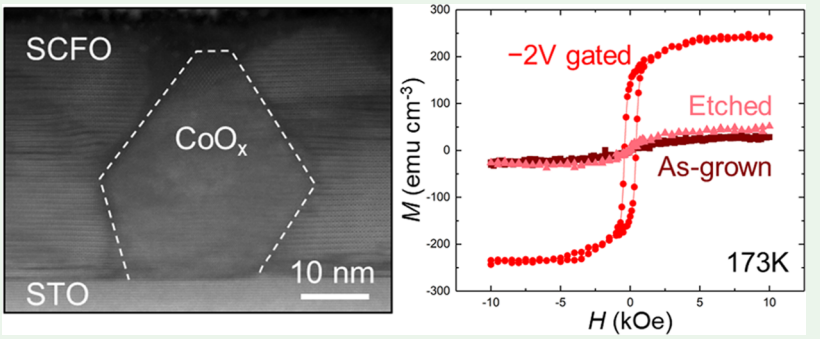

ABSTRACT: $SrCo_{1-x}Fe_xO_{3-\delta}$ (SCFO) grown on $SrTiO_3$ substrates using pulsed laser deposition forms either a single-phase film or a two-phase self-assembled nanocomposite film depending on the oxygen partial pressure, P_{O2}. A high P_{O2} of 150 mTorr during growth promotes phase separation of SCFO into a nanocomposite comprising Co oxide pillars embedded epitaxially in a Fe-rich SCFO matrix made up of brownmillerite and oxygen-deficient perovskite, despite the average composition of Sr/(Co + Fe) = 1. The SCFO matrix in the nanocomposite consists of a brownmillerite structure at a high Co content and an oxygen vacancy ordered perovskite at a high Fe content. In contrast, single-phase SCFO films grow at 20 mTorr. Ionic liquid gating of the nanocomposites oxidizes brownmillerite into perovskite with interlayer defects and renders the matrix phase magnetic with a saturation magnetization of 200 emu cm^{-3} at 173 K when x = 0.30.

KEYWORDS: *self-assembled nanocomposite, pulsed laser deposition, thin film growth, complex oxides, ionic liquid gating, voltage-controlled magnetism*

INTRODUCTION

Among the vast range of perovskite oxides, $SrCo_{1-x}Fe_xO_{3-\delta}$ (SCFO) is known as a mixed conductor useful in electrochemical applications such as solid oxide fuel cells, oxygen sensors, or oxygen separation membranes.[1,2] SCFO represents a solid solution of $SrCoO_{3-\delta}$ (SCO) and $SrFeO_{3-\delta}$ (SFO). The end members SCO and SFO show topotactic phase transitions from perovskite (P) to brownmillerite (BM, δ = 0.5), which can be induced by annealing,[3] an electrical stimulus,[4,5] or electrochemically via liquid electrolyte gating,[6,7] where an electric field is used to drive migration of O^{2-} or H^+ ions into a film.[8−10] Perovskite SCO (P-SCO) is a ferromagnet with Curie temperature T_C = 222 K,[11] and P-SFO is an antiferromagnet with a Néel temperature of T_N = 130 K,[12] whereas BM-SCO and BM-SFO are antiferromagnets with T_N = 570 and 715 K, respectively.[13,14] SCFO with Co/Fe ratios near 1:1 undergoes a reversible transition from ferromagnetic P to paramagnetic BM phases at room temperature by ionic liquid gating.[6]

The functionality of perovskite films can be extended by incorporation into self-assembled nanocomposites consisting of pillars or crystals of one phase, typically with a length scale of ca. 10−100 nm, embedded in a matrix of a second phase. Nanocomposites exhibit the properties of both phases and often reveal interfacially mediated cross-coupling between those properties, for example, magnetoelectric coupling in a nanocomposite consisting of a ferroelectric phase and a magnetic phase.[15−21] Nanocomposites have been synthesized from many combinations of materials, most commonly perovskite (e.g., $BiFeO_3$, $BaTiO_3$, $PbTiO_3$, $SrTiO_3$, $La_{0.8}Sr_{0.2}CoO_3$) and spinel (e.g., $CoFe_2O_4$, $MgFe_2O_4$, $NiFe_2O_4$, $Mn_{0.5}Zn_{0.5}Fe_2O_4$),[15,22−26] but have also included ZnO,[27] Sm_2O_3,[28] Cu oxides,[29] and metal nanowires or

Received: July 11, 2022
Accepted: September 12, 2022
Published: September 26, 2022

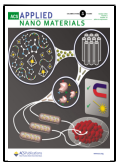

https://doi.org/10.1021/acsanm.2c03019
ACS Appl. Nano Mater. 2022, 5, 14646−14653

Scheme 1. Visual Description of PLD Combinatorial Growth Process Illustrating How P_{O2} during Growth Affects the Structure of Thin Films

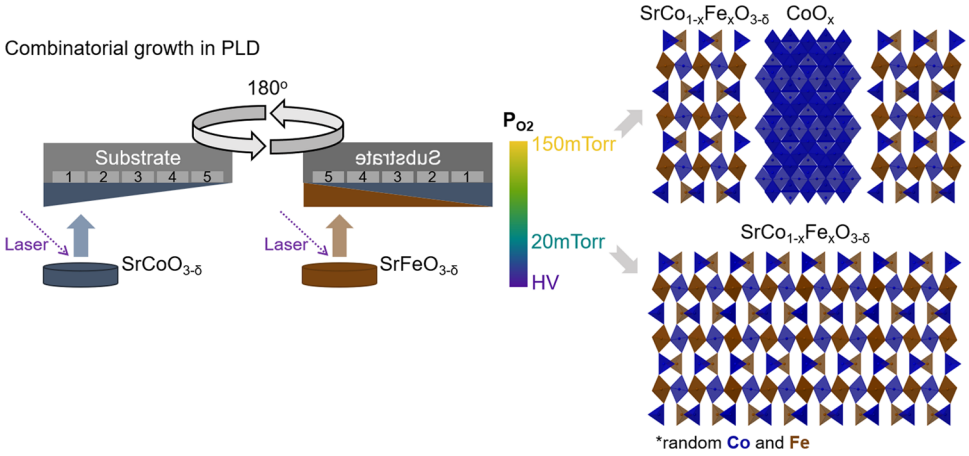

nanoparticles.[30,31] In our prior work, pulsed laser codeposition from SCO and Fe_3O_4 targets was used to form a nanocomposite consisting of an SCFO matrix and Co spinel (Co_3O_4) pillars of diameter ~50 nm, where the coherent interfaces enable strain transfer between the two phases.[6]

We show here that SCFO can be grown either as a single-phase film of perovskite or brownmillerite or as a two-phase nanocomposite with an additional cobalt oxide (CoO_x) phase present as <30 nm diameter pillars through control of oxygen pressure P_{O2} during pulsed laser deposition (PLD), with concomitant effects on its structure and magnetic properties. Single-phase films of SCFO form at intermediate P_{O2}, whereas two-phase nanocomposite films form at low or high P_{O2}. The formation of the nanocomposites is unexpected because the overall Sr:(Co + Fe) ratio of the film is 1:1, and the presence of CoO_x therefore implies that the SCFO phase is enriched in Sr. Finally, we describe how the structure and magnetic properties of the resulting films are modified by ionic liquid gating. The nanocomposite films may be useful in spintronic applications requiring electrically controlled magnetization, and the spontaneous formation of more than one oxide phase enables the introduction of multiple functionalities to the film.

EXPERIMENTAL SECTION

SCFO films and nanocomposites were grown on (001)-oriented $SrTiO_3$ (STO) substrates by PLD using a KrF excimer laser (λ = 248 nm) at a 5 Hz repetition rate with a fluence 1.3 J/cm^2. SCO and SFO targets were ablated at up to 60 shots each cycle, ensuring that the thickness of each deposited sublayer is less than that of a single unit cell. Ablation from two targets was used for convenient control of the Co/Fe ratio. The heater setpoint was 850 °C with the actual substrate temperature ~150 °C lower at ~700 °C, and the P_{O2} ranged from high vacuum (HV, P_{O2} <5 × 10^{-6} Torr) to 150 mTorr. Some samples were grown at 750 °C setpoint temperature (substrate temperature ~500 °C) and 2 J/cm^2 in a different chamber. The films were cooled down to room temperature in the same P_{O2} at a 20 °C/min cooling rate.

The crystal structure was characterized by high-resolution X-ray diffraction (XRD) using a Rigaku Smartlab high-resolution diffractometer with Ge-(220) double-bounce monochromator and a Cu Kα_1 (λ = 1.5406 Å) X-ray source. The morphology of the film was imaged with a Zeiss Merlin high-resolution scanning electron microscope (SEM). Nanocomposite films were etched in 10% HCl solution for 5 s to remove the matrix and leave the pillars. The chemical composition was obtained by wavelength-dispersive spectroscopy (WDS) using a JEOL-JXA-8200 Superprobe and Thermo Scientific K-Alpha X-ray photoelectron spectroscopy (XPS) system with Al Kα (1486.6 eV) as a source. The samples were coated with carbon for conductivity when performing WDS analysis. Before the XPS measurement, the sample surface was cleaned with a cluster ion beam for 30 s.

Lamella samples of the films along the [110] axis (indexed with respect to the axes of the cubic unit cell of P and the pseudocubic unit cell of BM) before and after ionic liquid gating were prepared for electron microscopy either using a Ga^+ ion beam in an FEI Helios Nanolab 600/660 Dual Beam system or by mechanical polishing. The samples were further thinned using Ar^+-ion milling. Scanning transmission electron microscopy (STEM) imaging and spectroscopy (energy-dispersive X-ray spectroscopy, EDS) analysis were performed on a probe-corrected Thermo Fisher Scientific Titan G3 60−300 kV microscope operated at 200 kV at a beam current of about 60 pA and convergence semiangle of 19.2 mrad. High-angle annular dark-field (HAADF) images were collected with a collection semiangle range of 65−200 mrad.

Ionic liquid gating was carried out to modify the structure and magnetic properties.[6] Experiments were done with 1-hexyl-3-methylimidazolium bis-(trifluoromethylsulfonyl)imide (HMIM-TFSI) as the electrolyte (Sigma-Aldrich). The films were immersed in the ionic liquid, a Pt probe was placed in direct contact with the sample surface, and a spiral Pt wire served as a counter electrode. A Hewlett-Packard 6632A power supply was used to apply the voltage during gating. The samples were gated at a negative bias of −2 V for 30 min to insert oxygen. The magnetic hysteresis loops were measured using a Digital Measurement System 7035B vibrating sample magnetometer (VSM) at room temperature and 173 K. Low temperature was obtained by flowing cold nitrogen gas past the sample from a liquid nitrogen source.

RESULTS AND DISCUSSION

In this study, P_{O2} and Fe content x are the primary variables affecting the film structure and phase formation. P_{O2} plays an important and complex role in PLD, determining the film lattice parameter, strain state, cation ratio and oxygen vacancy concentrations,[32−34] and differential scattering of the species in the plume.[35] P_{O2} also affects the surface roughness of the film,[33] influences the kinetic energy and oxidation state of arriving ions,[36] and alters the surface of the substrate;[37] furthermore, annealing in oxygen after growth can reduce[8] or oxidize[38,39] the film. In this work, films with different Co/Fe ratios, i.e., $(1-x)/x$, are produced by combinatorial growth, and two different growth modes (single- or two-phase films) can be obtained by controlling P_{O2}, as depicted in Scheme 1.

https://doi.org/10.1021/acsanm.2c03019
ACS Appl. Nano Mater. 2022, 5, 14646−14653

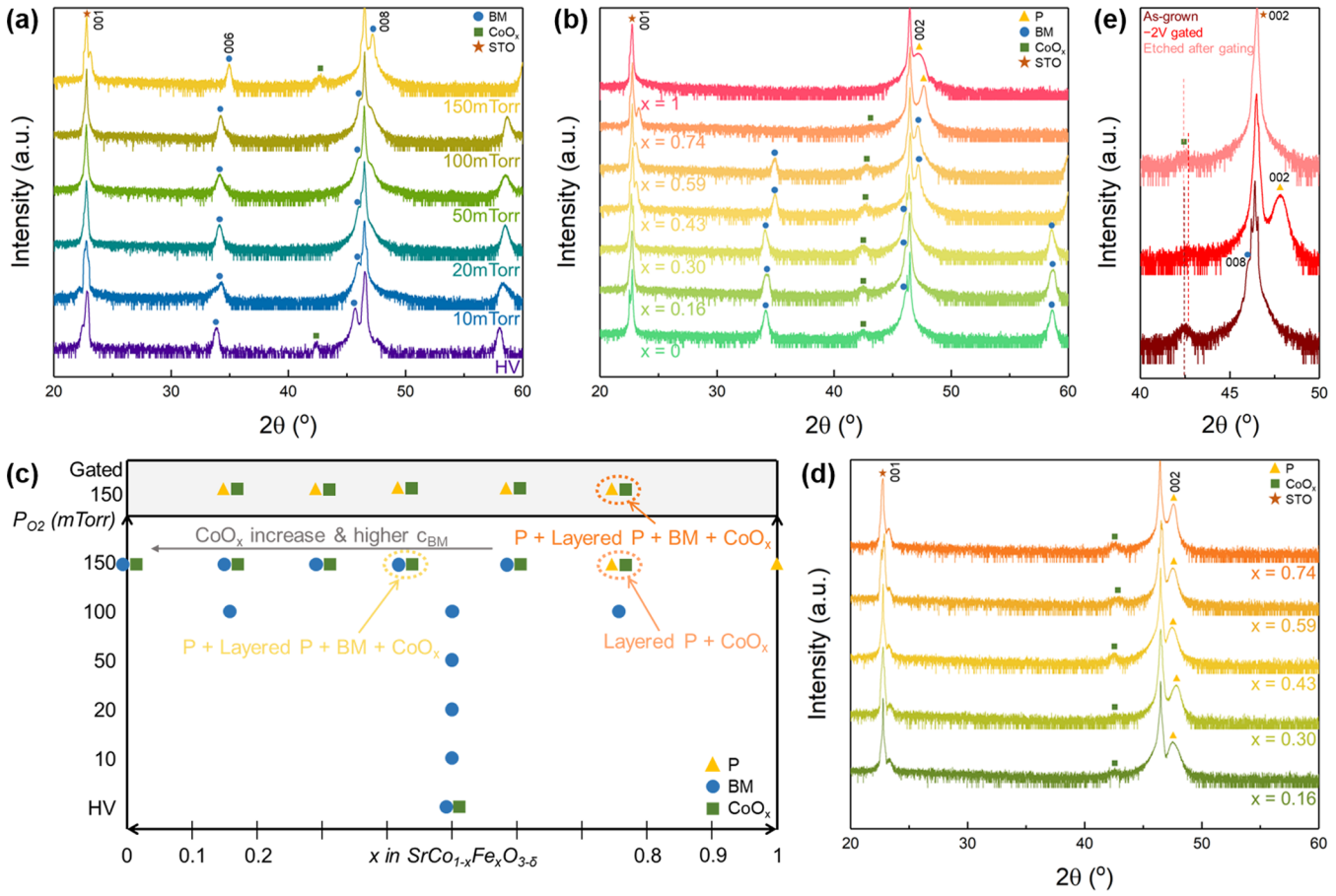

Figure 1. XRD results of (a) SCFO with $x \approx 0.5$ grown with P_{O2} = HV, 10, 20, 50, 100, and 150 mTorr, (b) SCFO at 150 mTorr with different x, (c) summary of phases present in films as a function of composition, oxygen pressure, and ionic liquid gating (circled samples were analyzed by STEM), (d) XRD pattern after −2 V gating of nanocomposite films grown at 150 mTorr, and (e) XRD pattern of SCFO with x = 0.30: as-grown, −2 V gated, and etched (x refers to the nominal composition).

To study the effect of P_{O2} on phase formation, we first vary P_{O2} from high vacuum (HV) to 150 mTorr during the growth of SCFO with $x \approx 0.5$, i.e., $SrFe_{0.5}Co_{0.5}O_{3-\delta}$ (Figure 1a). Films were deposited on STO substrates held at a temperature of ~700 °C, using a 5 Hz repetition rate and a laser fluence of 1.3 J/cm^2. For a total number of 12k laser shots, half from each target, the thickness of the film grown at 150 mTorr was 43.4 ± 1.1 nm based on XRD fitting (Figure S1, Supporting Information). At P_{O2} = 20 mTorr, a single-phase BM film is obtained, but at the extremes in pressure, i.e., HV and 150 mTorr, XRD peaks are observed from both the BM phase and a weaker spinel phase at $2\theta = 42°$.[6] At other pressures (10, 50, and 100 mTorr), the BM peak splits but no secondary phases are observed. The BM peak position moves to a higher angle when P_{O2} increases, clearly evident by comparison of the 150 mTorr and the HV samples, which is consistent with fewer oxygen vacancies, a higher cation oxidation state, and a smaller unit cell volume at a higher P_{O2}.[40]

These results indicate a process window for the formation of a single-phase SCFO film with x ≈ 0.5 at an optimum P_{O2} of 20 mTorr. We also prepared films at a lower substrate temperature (~500 °C) and a higher fluence (~2 J/cm^2) and found that SCFO grown at 20 mTorr and then annealed at P_{O2} = 0.1 mTorr or without O_2 also showed a two-phase film. Further description of these films can be found in Figure S2 (Supporting Information). This shows that the transition between forming single-phase and two-phase films depends on a combination of process parameters.

150 mTorr samples were then grown to investigate the structure and composition of the two-phase film as a function of Co/Fe ratio in $SrCo_{1-x}Fe_xO_{3-\delta}$ (Figure 1b). These films (grown at ~700 °C, 5 Hz, 1.3 J/cm^2) showed the presence of BM plus spinel phases for x = 0 to 0.59, perovskite plus a very weak spinel peak at x = 0.74, and only P phase for x = 1. Therefore, films with higher Co content favor two-phase microstructures.

As the Fe content increases, the lattice parameter of the BM phase becomes smaller. This observation is consistent with a larger population of higher valence, smaller radius Fe cations, and fewer oxygen vacancies. (If Fe and Co had the same valence state, films richer in Fe would have a larger lattice parameter because the ionic radius of Fe is larger than that of Co.) These trends contrast with observations in single-phase BM-SCFO films grown at 0.1 mTorr, where the out-of-plane lattice parameter increased with increasing Fe content.[6] The spinel peak also shifts slightly with varying composition, consistent with some level of interfacial coherency between the two phases.

To determine the morphology of the two-phase films, we etch with 10% HCl solution to remove the matrix phase. For the samples of x = 0.30 and x = 0.59, etching leaves free-standing rectangular or square-based pillars growing vertically through the film thickness with an average edge length of ~17

https://doi.org/10.1021/acsanm.2c03019
ACS Appl. Nano Mater. 2022, 5, 14646−14653

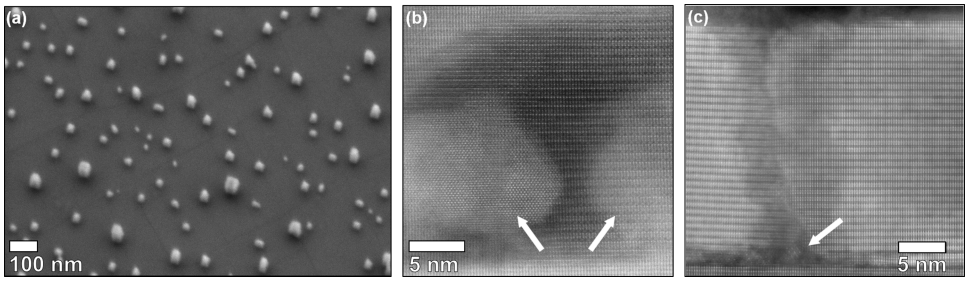

Figure 2. (a) SEM image of the etched $x = 0.30$ film with 30° tilt angle showing pillars; (b, c) HAADF-STEM images of (b) as-grown $x = 0.43$ film with pillars (marked by arrows) surrounded by the matrix and (c) as-grown $x = 0.74$ film showing the nucleation of Co_3O_4 between the substrate/film interface and film grain boundary, marked by the arrow.

nm (range of 8−30 nm), as shown in Figures 2a and S3a (Supporting Information). Smaller crystals with size below 10 nm were also present on the substrate, indicating that a higher density of crystals nucleated at the start of film growth, but not all crystals continued to grow as high as the film thickness. By analogy with other spinel-perovskite composites grown on STO, the crystals are identified as spinel and the matrix as perovskite, i.e., SCFO. The as-grown $x = 0.43$ sample was imaged in cross section using HAADF-STEM (Figure 2b) along the [110] axis and showed typical (111) facets of the spinel phase. The $x = 0.74$ sample (Figure 2c) in cross section showed nucleation of small pillars at the substrate and film interface, consistent with the barely detectable spinel peak shown in Figure 1b. Its perovskite matrix exhibits a layered structure, which is attributed to oxygen vacancy ordering and will be described in detail elsewhere.[41]

These results indicate that the SCFO samples grown at 150 mTorr are vertically aligned nanocomposites made up of a BM (for high Co content) and/or P (for high Fe content) matrix and an increasing amount of spinel pillars for higher Co content. As a comparison, we also grew films at 100 mTorr, and these only exhibited BM without detectable amounts of spinel phases (Figure S4, Supporting Information). The phases present in the films are summarized in Figure 1c as a function of Co/Fe ratio and P_{O2}.

Compositional mapping of the $x = 0.74$, 150 mTorr sample in Figure 3a indicates that the pillars contain little or no Fe, and therefore consist of cobalt oxide, CoO_x. The preferential incorporation of Co in the spinel and Fe remaining in the perovskite have been seen in other studies, such as the formation of CoO and Co_3O_4 during the deposition of a composite of $La_{0.6}Sr_{0.4}CoO_3$ and $CoFe_2O_4$,[42] and SCFO and Co_3O_4 phases produced during codeposition from SCO and Fe_3O_4 targets.[6] Moreover, comparing Figures S3b,c (Supporting Information), the number and area density of pillars exposed on the surface decrease as the Fe content increases. We conclude that the key factor promoting the formation of a nanocomposite from SCO+SFO codeposition at a high P_{O2} is the presence of Co.

XPS survey scan results for the nanocomposite films grown at $P_{O2} = 150$ mTorr show that the Sr/(Co + Fe) ratio is close to 1 (Figure S5, Supporting Information). Moreover, quantitative analysis of the STEM EDS scan (Figure 3a) gives Sr of 48 ± 9%, Co of 13 ± 2%, and Fe of 39 ± 6%, consistent with Sr/(Co + Fe) = 1 within the error bars. We note that WDS was not appropriate for Sr/(Co + Fe) determination because of the Sr contribution from the STO substrate. This implies that a stoichiometry change due to differential scattering between the species is not likely to be responsible for the emergence of the spinel phase. A pseudo-ternary phase diagram of SrO-CoO-FeO at 900 °C in air[43] shows that SCFO exhibits complete solid solubility across the range of Co/Fe ratio, but a deficiency in Sr promotes the formation of secondary phases $Co_{3-y}Fe_yO_4$ and $Sr_4Co_zFe_{6-z}O_{13}$. Furthermore, the phase diagram in ref 43 implies that SCFO cannot coexist with $CoFe_2O_4$ thermodynamically at 900 °C in air, whereas SCFO and $Co_{3-y}Fe_yO_4$ can readily coexist up to 900 °C depending on the cobalt content. The high Co content of the spinel phase of the nanocomposites is consistent with these phase equilibria. Therefore, we attribute the formation of the two-phase nanocomposite in our study to the thermodynamic stability of the spinel Co_3O_4 phase. Nucleation of the stable CoO_x could be facilitated by columnar growth of the film, which is favored at a high P_{O2}.[34]

The CoO_x formation implies an excess of Sr in the remaining SCFO matrix phase. Considering the approximate volume fraction of the pillars (1%) in the $x = 0.30$ sample, the SCFO matrix has a Sr:(Co + Fe) ratio of roughly 1:0.95. This may be accommodated by Sr_{Fe} or Sr_{Co} antisite defects (associated with additional oxygen vacancies (V_O) for charge balance) analogous to the behavior of Ti-deficient STO epitaxial films,[44] or as B-site vacancies (here V_{Fe} or V_{Co}) as in La-rich $LaAlO_3$ films.[45] Larger Sr excess may lead to the formation of Ruddlesden−Popper layered phases ($Sr_{n+1}(Co,Fe)_nO_{3n+1}$, with n an integer), which has been reported for highly Ti-deficient STO,[46] but the Sr content here is presumably not large enough to produce these phases.

We performed −2 V ionic liquid gating on the five nanocomposite samples grown at 150 mTorr to oxidize them and to promote ferromagnetic exchange interaction between Co/Fe. According to the XRD pattern in Figure 1d, gating converts the BM to P while preserving the spinel peak and does not produce a spinel peak in other samples that did not originally have one. The film shows a metallic finish as the insulating BM converts to conductive P. Gating changes the out-of-plane lattice parameter of the matrix by −3% and that of the pillars by around −1% due to strain transferred from the matrix (Figure 1e). In ref 6, single-phase BM-$SrCo_{1-y}Fe_yO_{2.5}$ was oxidized into P-$SrCo_{1-y}Fe_yO_3$, and different initial compositions, y, yielded different final lattice parameters after gating. In contrast, here, we observe that the lattice parameter of the gated SCFO matrix is the same for $x = 0.16$ to $x = 0.74$. This may indicate less variability in the Co/Fe ratio in the matrix due to the precipitation of CoO_x secondary phase and also reflect the influence of vertical epitaxy on constraining the lattice parameter of the matrix because reciprocal space mapping suggests that the matrix is strained in-plane on the substrate.[41]

https://doi.org/10.1021/acsanm.2c03019
ACS Appl. Nano Mater. 2022, 5, 14646−14653

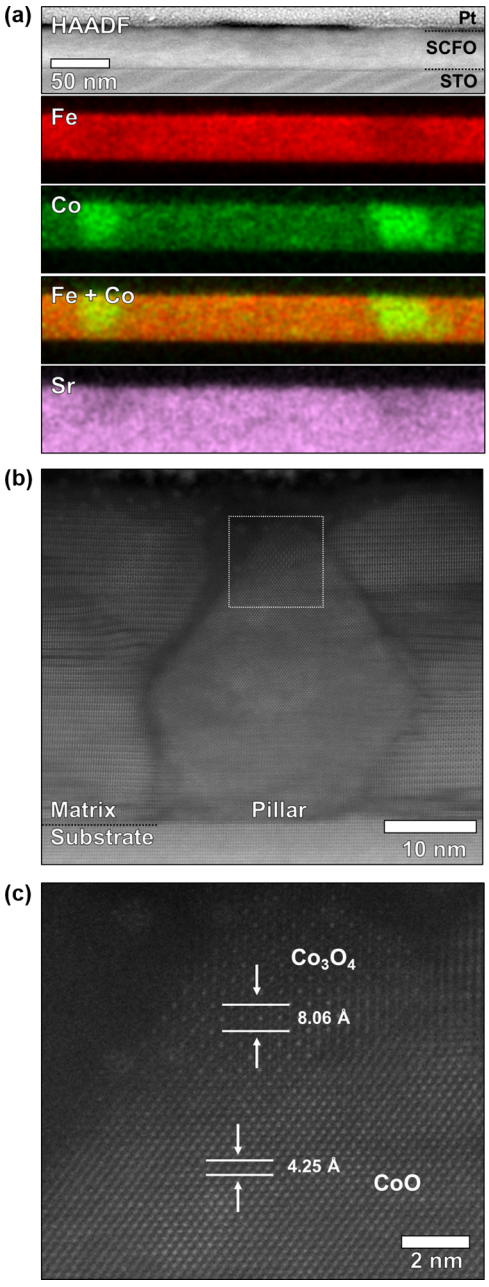

Figure 3. (a) STEM EDS elemental maps of an $x = 0.74$ film after −2 V gating, (b) HAADF-STEM image showing a pillar at center and the layered oxygen-deficient P matrix, and (c) magnified image of the outlined region in (b) with the atomic distance of Co_3O_4 and CoO indicated.

The bias voltage did not play a significant role in gating as long as it is beyond the threshold for the water molecules to decompose and provide the oxygen that enables the phase change. Applying +2 V after −2 V gating to the nanocomposite turns P back to BM (Figure S6, Supporting Information), but 30 min was not sufficient to fully transform the matrix unlike the single-phase shown in ref 6.

HAADF-STEM measurements of the gated $x = 0.74$ sample (Figure S7, Supporting Information) show that the top region of the matrix is mostly P. The matrix closer to the substrate retains its as-grown structure which is layered P, and BM exists near the spinel pillars where it is assumed to accommodate the structural distortion caused by the vertices of the (111) facet of the pillars since BM has a larger lattice parameter. The BM does not produce a measurable subpeak in XRD either before or after gating; it may have been present in the film even before gating but at such a low fraction that it does not yield peaks in XRD. In addition, the ionic liquid gating induced defects in the matrix phase evident as dark lines parallel to the substrate separating and distorting the lattice planes. This is also evident in the deterioration of the rocking curve (Figure S8, Supporting Information). Furthermore, we find that the Co-rich pillar includes regions of rocksalt CoO as well as spinel (Figure 3b,3c), but these could not be distinguished in XRD. The direction of gating would oxidize CoO into Co_3O_4; thus, the CoO was likely present as grown. Therefore, for the $x = 0.74$ sample grown at 150 mTorr, while the XRD indicates that spinel and perovskite are present before and after gating, STEM indicates a more complex structure in which the matrix consists of perovskite, layered perovskite, and a small amount of brownmillerite with pillars consisting of Co_3O_4 and CoO.

The Co-rich composition of the spinel phase is confirmed by magnetization measurements. The as-grown nanocomposite has no room-temperature magnetic moment (Figure S9, Supporting Information), which excludes the composition of the spinel phase being $CoFe_2O_4$ or Fe_3O_4, both of which are magnetic at room temperature. Compared with magnetic data from $(Co,Fe)_3O_4$ nanoparticles,[47] the upper bound for Fe content in our pillars is $Co_{1.6}Fe_{1.4}O_4$, and it is likely much lower (close to zero Fe) according to the compositional analysis.

Figure 4a shows the in-plane hysteresis loops measured at 173 K for as-grown, −2 V gated, and etched nanocomposites with $x = 0.30$ grown at $P_{O2} = 150$ mTorr. The magnetic moment appears on gating but disappears on etching the matrix, indicating that the magnetism originates from the gated SCFO phase and not the pillars.[6] The saturation magnetization (M_s) of the gated nanocomposite was 200 emu cm^{-3} at 173 K but 20 emu cm^{-3} at room temperature, suggesting that its T_C is just above room temperature. Similarly, the $x = 0.59$ nanocomposite has an M_s of 300 emu cm^{-3} at 173 K after gating but a negligible moment at room temperature (Figure S10, Supporting Information). The −2 V gating does not produce significant magnetism at room temperature, which implies that the matrix Co/Fe ratio has deviated from 1:1 because of the precipitation of CoO_x.[6] In comparison, single-phase film ($P_{O2} = 20$ mTorr) after gating shows a maximum M_s of 100 emu cm^{-3} at room temperature and $T_C = 340$ K for $x = 0.5$ (Figure 4b), and both M_s and T_C fall as compositions deviate from $x = 0.5$; at 173 K, a single-phase gated sample with $x = 0.3$ gave M_s ~150 emu cm^{-3}.[6] The higher M_s of the gated nanocomposite at 173 K suggests that its matrix has $x > 0.3$, which is consistent with the Co being present in the pillar phases and Fe being enriched in the matrix compared to the average composition. These results show that spinel-perovskite nanocomposites consisting of a magnetic matrix and paramagnetic pillars are created by gating SCFO grown at high P_{O2}.

CONCLUSIONS

This work shows that codeposition from SCO and SFO targets can produce either a single-phase SCFO film or a two-phase nanocomposite film, depending on the oxygen pressure during growth. The formation of the nanocomposite is unanticipated because the film cation ratio is stoichiometric for perovskite and brownmillerite, i.e., Sr/(Co + Fe) = 1, so it is not driven by the presence of excess Co and Fe as in the case of

https://doi.org/10.1021/acsanm.2c03019
ACS Appl. Nano Mater. 2022, 5, 14646−14653

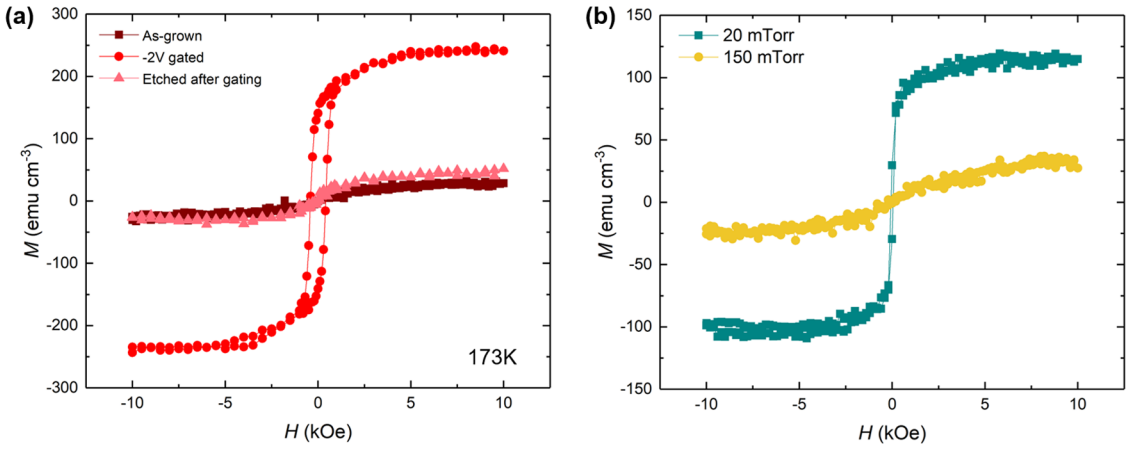

Figure 4. In-plane M-H loops of (a) $x = 0.30$ sample measured at 173 K as-grown, −2 V gated, and etched; (b) two $x \approx 0.5$ samples measured at room temperature after −2 V gating. These samples were grown at 20 mTorr (green: single-phase, T_C above room temperature) and 150 mTorr (yellow: nanocomposite, matrix has a higher Fe content and a lower T_C).

nanocomposites formed by codeposition from spinel and perovskite targets. Nanocomposite formation in our case appears to be favored by the thermodynamic stability of cobalt oxide phases, and the volume fraction of pillars increases with Co content. The excess Sr is likely incorporated into the matrix via antisite defects and additional oxygen vacancies. The SCFO forms a brownmillerite matrix phase at a high Co content and perovskite phases at a high Fe content.

STEM reveals that the nanocomposites contain several phases, in which oxygen-deficient P and BM coexist in the matrix, and spinel and rocksalt Co oxides in the pillars. The Co/Fe composition of the matrix defines its response to ionic liquid gating and its magnetic properties. Gating converts BM into P for all compositions, but the P formed by gating contains defects where the layered structure is disrupted, and some BM remains near the pillars. The magnetic moment of the nanocomposites originates from the matrix and increases on gating as BM is converted to P; however, the magnetic moment differs from that found by gating of single-phase BM-SCFO to P-SCFO because the matrix in the nanocomposite film contains more Fe than the nominal composition. Strain coupling between the matrix and pillar is evident by the shift in XRD peak position upon gating.

This work shows that self-assembled oxide nanocomposites, typically formed by the codeposition of two different phases, can instead be formed in a film with a stoichiometric perovskite cation ratio by selecting the processing parameters. The oxygen pressure during growth, P_{O2}, has a profound influence on the oxide film morphology and the phase stability of nanocomposite thin films. These nanocomposites may be favorable for applications that require multifunctionality in a single film, or electrical control of magnetism, e.g., magneto-electric memory.

■ ASSOCIATED CONTENT

Supporting Information

The Supporting Information is available free of charge at https://pubs.acs.org/doi/10.1021/acsanm.2c03019.

XRD thickness fitting of SCFO; XRD and SEM images of SCFO films grown at higher fluence; SEM images of as-grown and etched SCFO nanocomposites; XRD pattern of SCFO grown at 100 mTorr; XPS survey scan and semiquantitative analysis; XRD pattern of −2 V then +2 V gated SCFO nanocomposites; STEM images after ionic liquid gating of SCFO nanocomposite; rocking curve comparison before and after gating; magnetic hysteresis loops of as-grown SCFO films; magnetic hysteresis loops of −2 V gated SCFO films; and XRD pattern of as-grown and gated Co_3O_4/STO (PDF)

■ AUTHOR INFORMATION

Corresponding Authors

Shuai Ning − *School of Materials Science and Engineering, National Institute for Advanced Materials, Nankai University, Tianjin 300350, People's Republic of China;* orcid.org/0000-0002-2840-7270; Email: sning@nankai.edu.cn

Caroline A. Ross − *Department of Materials Science and Engineering, Massachusetts Institute of Technology, Cambridge, Massachusetts 02139, United States;* orcid.org/0000-0003-2262-1249; Email: caross@mit.edu

Authors

Eunsoo Cho − *Department of Materials Science and Engineering, Massachusetts Institute of Technology, Cambridge, Massachusetts 02139, United States;* orcid.org/0000-0002-0740-0192

Abinash Kumar − *Department of Materials Science and Engineering, Massachusetts Institute of Technology, Cambridge, Massachusetts 02139, United States*

James M. LeBeau − *Department of Materials Science and Engineering, Massachusetts Institute of Technology, Cambridge, Massachusetts 02139, United States*

Complete contact information is available at: https://pubs.acs.org/10.1021/acsanm.2c03019

Notes

The authors declare no competing financial interest.

■ ACKNOWLEDGMENTS

The authors gratefully acknowledge the support of NSF award 1911792 and the use of shared experimental facilities of the MRSEC Program of the National Science Foundation, award DMR-1419807. Sample preparation for electron microscopy is

performed at the Harvard University Center for Nanoscale Systems (CNS), a member of the National Nanotechnology Coordinated Infrastructure Network (NNCI), which is supported by the National Science Foundation under NSF Grant No. 1541959. A.K. and J.M.L. acknowledge support from ARL/ARO via the Collaborative for Hierarchical Agile and Responsive Materials (CHARM), under Cooperative Agreement No. W911NF-19-2-0119. This work was carried out in part through the use of the MIT Characterization.nano facility. S.N. acknowledges support from the National Natural Science Foundation of China (grant no. 52102135).

REFERENCES

(1) Grunbaum, N.; Mogni, L.; Prado, F.; Caneiro, A. Phase Equilibrium and Electrical Conductivity of SrCo0.8Fe0.2O3-δ. *J. Solid State Chem.* **2004**, *177*, 2350−2357.
(2) Ma, B.; Victory, N. I.; Balachandran, U.; Mitchell, B. J.; Richardson, J. W., Jr. Study of the Mixed-Conducting SrFeCo0.5Oy System. *J. Am. Ceram. Soc.* **2004**, *85*, 2641−2645.
(3) Jeen, H.; Choi, W. S.; Biegalski, M. D.; Folkman, C. M.; Tung, I. C.; Fong, D. D.; Freeland, J. W.; Shin, D.; Ohta, H.; Chisholm, M. F.; Lee, H. N. Reversible Redox Reactions in an Epitaxially Stabilized SrCoOx Oxygen Sponge. *Nat. Mater.* **2013**, *12*, 1057−1063.
(4) Acharya, S. K.; Nallagatla, R. V.; Togibasa, O.; Lee, B. W.; Liu, C.; Jung, C. U.; Park, B. H.; Park, J. Y.; Cho, Y.; Kim, D. W.; Jo, J.; Kwon, D. H.; Kim, M.; Hwang, C. S.; Chae, S. C. Epitaxial Brownmillerite Oxide Thin Films for Reliable Switching Memory. *ACS Appl. Mater. Interfaces* **2016**, *8*, 7902−7911.
(5) Tian, J.; Wu, H.; Fan, Z.; Zhang, Y.; Pennycook, S. J.; Zheng, D.; Tan, Z.; Guo, H.; Yu, P.; Lu, X.; Zhou, G.; Gao, X.; Liu, J. M. Nanoscale Topotactic Phase Transformation in SrFeOx Epitaxial Thin Films for High-Density Resistive Switching Memory. *Adv. Mater.* **2019**, *31*, 1−11.
(6) Ning, S.; Zhang, Q.; Occhialini, C.; Comin, R.; Zhong, X.; Ross, C. A. Voltage Control of Magnetism above Room Temperature in Epitaxial SrCo1−xFexO3−δ. *ACS Nano* **2020**, *14*, 8949−8957.
(7) Ge, C.; Liu, C. x.; Zhou, Q. l.; Zhang, Q. h.; Du, J. y.; Li, J. k.; Wang, C.; Gu, L.; Yang, G. z.; Jin, K. j. A Ferrite Synaptic Transistor with Topotactic Transformation. *Adv. Mater.* **2019**, *31*, 1900379.
(8) Saleem, M. S.; Cui, B.; Song, C.; Sun, Y.; Gu, Y.; Zhang, R.; Fayaz, M. U.; Zhou, X.; Werner, P.; Parkin, S. S. P.; Pan, F. Electric Field Control of Phase Transition and Tunable Resistive Switching in SrFeO2.5. *ACS Appl. Mater. Interfaces* **2019**, *11*, 6581−6588.
(9) Lu, N.; Zhang, P.; Zhang, Q.; Qiao, R.; He, Q.; Li, H. B.; Wang, Y.; Guo, J.; Zhang, D.; Duan, Z.; Li, Z.; Wang, M.; Yang, S.; Yan, M.; Arenholz, E.; Zhou, S.; Yang, W.; Gu, L.; Nan, C. W.; Wu, J.; Tokura, Y.; Yu, P. Electric-Field Control of Tri-State Phase Transformation with a Selective Dual-Ion Switch. *Nature* **2017**, *546*, 124−128.
(10) Li, H. B.; Lou, F.; Wang, Y.; Zhang, Y.; Zhang, Q.; Wu, D.; Li, Z.; Wang, M.; Huang, T.; Lyu, Y.; Guo, J.; Chen, T.; Wu, Y.; Arenholz, E.; Lu, N.; Wang, N.; He, Q.; Gu, L.; Zhu, J.; Nan, C. W.; Zhong, X.; Xiang, H.; Yu, P. Electric Field-Controlled Multistep Proton Evolution in HxSrCoO2.5 with Formation of H−H Dimer. *Adv. Sci.* **2019**, *6*, 1901432.
(11) Taguchi, H.; Shimada, M.; Koizumi, M. The Effect of Oxygen Vacancy on the Magnetic Properties in the System SrCoO3-δ (0 < δ < 0.5). *J. Solid State Chem.* **1979**, *29*, 221−225.
(12) MacChesney, J. B.; Sherwood, R. C.; Potter, J. F. Electric and Magnetic Properties of the Strontium Ferrates. *J. Chem. Phys.* **1965**, *43*, 1907−1913.
(13) Takeda, T.; Yamaguchi, Y.; Watanabe, H. Magnetic Structure of SrCoO2.5. *J. Phys. Soc. Jpn.* **1972**, *33*, 970−972.
(14) Grenier, J. C.; Ea, N.; Pouchard, M.; Hagenmuller, P. Structural Transitions at High Temperature in Sr2Fe2O5. *J. Solid State Chem.* **1985**, *58*, 243−252.
(15) Kim, D. H.; Ning, S.; Ross, C. A. Self-Assembled Multiferroic Perovskite-Spinel Nanocomposite Thin Films: Epitaxial Growth, Templating and Integration on Silicon. *J. Mater. Chem. C* **2019**, *7*, 9128−9148.
(16) Aimon, N. M.; Kim, D. H.; Choi, H. K.; Ross, C. A. Deposition of Epitaxial BiFeO3/CoFe2O4 Nanocomposites on (001) SrTiO3 by Combinatorial Pulsed Laser Deposition. *Appl. Phys. Lett.* **2012**, *100*, 092901.
(17) Ma, J.; Hu, J.; Li, Z.; Nan, C. W. Recent Progress in Multiferroic Magnetoelectric Composites: From Bulk to Thin Films. *Adv. Mater.* **2011**, *23*, 1062−1087.
(18) Misra, S.; Wang, H. Review on the Growth, Properties and Applications of Self-Assembled Oxide-Metal Vertically Aligned Nanocomposite Thin Films−Current and Future Perspectives. *Mater. Horiz.* **2021**, *8*, 869−884.
(19) Chen, A.; Su, Q.; Han, H.; Enriquez, E.; Jia, Q. Metal Oxide Nanocomposites: A Perspective from Strain, Defect, and Interface. *Adv. Mater.* **2019**, *31*, 1803241.
(20) Huang, J.; Li, W.; Yang, H.; MacManus-Driscoll, J. L. Tailoring Physical Functionalities of Complex Oxides by Vertically Aligned Nanocomposite Thin-Film Design. *MRS Bull.* **2021**, *46*, 159−167.
(21) Dix, N.; Muralidharan, R.; Guyonnet, J.; Warot-Fonrose, B.; Varela, M.; Paruch, P.; Sánchez, F.; Fontcuberta, J. On the Strain Coupling across Vertical Interfaces of Switchable BiFeO3-CoFe2O4 Multiferroic Nanostructures. *Appl. Phys. Lett.* **2009**, *95*, 062907.
(22) Kim, D. H.; Aimon, N. M.; Sun, X.; Ross, C. A. Compositionally Modulated Magnetic Epitaxial Spinel/Perovskite Nanocomposite Thin Films. *Adv. Funct. Mater.* **2014**, *24*, 2334−2342.
(23) Zhan, Q.; Yu, R.; Crane, S. P.; Zheng, H.; Kisielowski, C.; Ramesh, R. Structure and Interface Chemistry of Perovskite-Spinel Nanocomposite Thin Films. *Appl. Phys. Lett.* **2006**, *89*, 172902.
(24) Yang, Y.; Priya, S.; Wang, Y. U.; Li, J. F.; Viehland, D. Solid-State Synthesis of Perovskite-Spinel Nanocomposites. *J. Mater. Chem.* **2009**, *19*, 4998−5002.
(25) Kim, D. H.; Kim, T. C.; Lee, S. H.; Han, S. H.; Han, K. S.; Ross, C. A. Self-Assembled Growth of Sr(Ti,Fe)O3-CoFe2O4 Magnetic Nanocomposite Thin Films. *J. Appl. Phys.* **2017**, *121*, 163902.
(26) Chen, Y.; Ojha, S.; Tsvetkov, N.; Kim, D. H.; Yildiz, B.; Ross, C. A. Spinel/Perovskite Cobaltite Nanocomposites Synthesized by Combinatorial Pulsed Laser Deposition. *CrystEngComm* **2016**, *18*, 7745−7752.
(27) Fix, T.; Choi, E. M.; Robinson, J. W. A.; Lee, S. B.; Chen, A.; Prasad, B.; Wang, H.; Blamire, M. G.; Macmanus-Driscoll, J. L. Electric-Field Control of Ferromagnetism in a Nanocomposite via a ZnO Phase. *Nano Lett.* **2013**, *13*, 5886−5890.
(28) MacManus-Driscoll, J.; Suwardi, A.; Kursumovic, A.; Bi, Z.; Tsai, C. F.; Wang, H.; Jia, Q.; Lee, O. J. New Strain States and Radical Property Tuning of Metal Oxides Using a Nanocomposite Thin Film Approach. *APL Mater.* **2015**, *3*, 062507.
(29) Wang, Y.; Ghanbaja, J.; Bruyère, S.; Soldera, F.; Horwat, D.; Mücklich, F.; Pierson, J. F. Room Temperature Self-Assembled Growth of Vertically Aligned Columnar Copper Oxide Nanocomposite Thin Films on Unmatched Substrates. *Sci. Rep.* **2017**, *7*, No. 11122.
(30) Huang, J.; Li, L.; Lu, P.; Qi, Z.; Sun, X.; Zhang, X.; Wang, H. Self-Assembled Co-BaZrO3 Nanocomposite Thin Films with Ultra-Fine Vertically Aligned Co Nanopillars. *Nanoscale* **2017**, *9*, 7970−7976.
(31) Kim, D. H.; Sun, X. Y.; Aimon, N. M.; Kim, J. J.; Campion, M. J.; Tuller, H. L.; Kornblum, L.; Walker, F. J.; Ahn, C. H.; Ross, C. A. A Three Component Self-Assembled Epitaxial Nanocomposite Thin Film. *Adv. Funct. Mater.* **2015**, *25*, 3091−3100.
(32) Kumari, S.; Mottaghi, N.; Huang, C. Y.; Trappen, R.; Bhandari, G.; Yousefi, S.; Cabrera, G.; Seehra, M. S.; Holcomb, M. B. Effects of Oxygen Modification on the Structural and Magnetic Properties of Highly Epitaxial La0.7Sr0.3MnO3 (LSMO) Thin Films. *Sci. Rep.* **2020**, *10*, No. 3659.
(33) Eason, R. *Pulsed Laser Deposition of Thin Films*, Wiley, 2006.
(34) Chen, A. P.; Khatkhatay, F.; Zhang, W.; Jacob, C.; Jiao, L.; Wang, H. Strong Oxygen Pressure Dependence of Ferroelectricity in

https://doi.org/10.1021/acsanm.2c03019
ACS Appl. Nano Mater. 2022, 5, 14646−14653

BaTiO3/SrRuO3/SrTiO3 Epitaxial Heterostructures. *J. Appl. Phys.* **2013**, *114*, 124101.
(35) Lafane, S.; Kerdja, T.; Abdelli-Messaci, S.; Khereddine, Y.; Kechouane, M.; Nemraoui, O. Correlation of Plume Dynamics and Oxygen Pressure with VO2 Stoichiometry during Pulsed Laser Deposition. *Appl. Phys. A Mater. Sci. Process.* **2013**, *112*, 159−164.
(36) Aruta, C.; Amoruso, S.; Bruzzese, R.; Wang, X.; MacCariello, D.; Miletto Granozio, F.; Scotti Di Uccio, U. Pulsed Laser Deposition of SrTiO3/LaGaO3 and SrTiO3/LaAlO3: Plasma Plume Effects. *Appl. Phys. Lett.* **2010**, *97*, 3−6.
(37) Kang, K. T.; Zhang, B.; Sharma, Y.; Paudel, B.; Wang, H.; Dowden, P.; Chen, A. Substrate Oxygen Sponge Effect: A Parameter for Epitaxial Manganite Thin Film Growth. *Appl. Phys. Lett.* **2020**, *117*, 151601.
(38) Wang, Y.; He, Q.; Ming, W.; Du, M. H.; Lu, N.; Cafolla, C.; Fujioka, J.; Zhang, Q.; Zhang, D.; Shen, S.; Lyu, Y.; N'diaye, A. T.; Arenholz, E.; Gu, L.; Nan, C.; Tokura, Y.; Okamoto, S.; Yu, P. Robust Ferromagnetism in Highly Strained SrCoO3 Thin Films. *Phys. Rev. X* **2020**, *10*, 1−10.
(39) Hu, S.; Wang, Y.; Cazorla, C.; Seidel, J. Strain-Enhanced Oxygen Dynamics and Redox Reversibility in Topotactic SrCoO3-δ ($0 < \delta \leq 0.5$). *Chem. Mater.* **2017**, *29*, 708−717.
(40) Chen, J.; Döbeli, M.; Stender, D.; Lee, M. M.; Conder, K.; Schneider, C. W.; Wokaun, A.; Lippert, T. Tracing the Origin of Oxygen for La0.6Sr0.4MnO3 Thin Film Growth by Pulsed Laser Deposition. *J. Phys. D. Appl. Phys.* **2015**, *49*, 045201.
(41) Cho, E.; Kumar, A.; Ning, S.; LeBeau, J. M.; Ross, C. A. Oxygen Vacancy Ordering in Perovskite SrCo1-xFexO3-δ Films Made by Pulsed Laser Deposition. Manuscript in preparation.
(42) Hoffmann, J.; Schnittger, S.; Norpoth, J.; Raabe, S.; Kramer, T.; Jooss, C. Nanocomposite Stability in Fe-, Co-, and Mn-Based Perovskite/Spinel Systems. *J. Mater. Res.* **2012**, *27*, 1462−1470.
(43) Fossdal, A.; Sagdahl, L. T.; Einarsrud, M. A.; Wiik, K.; Grande, T.; Larsen, P. H.; Poulsen, F. W. Phase Equilibria and Microstructure in Sr4Fe6-xCoxO13 $0 \leq x \leq 4$ Mixed Conductors. *Solid State Ionics* **2001**, *143*, 367−377.
(44) Fuchs, D.; Adam, M.; Schweiss, P.; Gerhold, S.; Schuppler, S.; Schneider, R.; Obst, B. Structural Properties of Slightly Off-Stoichiometric Homoepitaxial SrTixO3-δ Films. *J. Appl. Phys.* **2000**, *88*, 1844−1850.
(45) Qiao, L.; Droubay, T. C.; Varga, T.; Bowden, M. E.; Shutthanandan, V.; Zhu, Z.; Kaspar, T. C.; Chambers, S. A. Epitaxial Growth, Structure, and Intermixing at the LaAlO3/SrTiO3 Interface as the Film Stoichiometry Is Varied. *Phys. Rev. B* **2011**, *83*, 085408.
(46) Tilley, R. J. D. An Electron Microscope Study of Perovskite-Related Oxides in the Sr-Ti-O System. *J. Solid State Chem.* **1977**, *21*, 293−301.
(47) Franco, A.; Zapf, V. Temperature Dependence of Magnetic Anisotropy in Nanoparticles of CoxFe(3-x)O4. *J. Magn. Magn. Mater.* **2008**, *320*, 709−713.

https://doi.org/10.1021/acsanm.2c03019
ACS Appl. Nano Mater. 2022, 5, 14646−14653